

Influence of circumferential solar heat flux distribution on the heat transfer coefficients of linear Fresnel collector absorber tubes

Izuchukwu F. Okafor, Jaco Dirker* and Josua P. Meyer**

Department of Mechanical and Aeronautical Engineering, University of Pretoria, Pretoria, Private Bag X20, Hatfield 0028, South Africa.

**Corresponding Author:*

Email Address: jaco.dirker@up.ac.za

Phone: +27 (0)12 420 2465

***Alternative Corresponding Author:*

Email Address: josua.meyer@up.ac.za

Phone +27 (0)12 420 3104

ABSTRACT

The absorber tubes of solar thermal collectors have enormous influence on the performance of the solar collector systems. In this numerical study, the influence of circumferential uniform and non-uniform solar heat flux distributions on the internal and overall heat transfer coefficients of the absorber tubes of a linear Fresnel solar collector was investigated. A 3D steady-state numerical simulation was implemented based on ANSYS Fluent code version 14. The non-uniform solar heat flux distribution was modelled as a sinusoidal function of the concentrated solar heat flux incident on the circumference of the absorber tube. The k- ϵ model was employed to simulate the turbulent flow of the heat transfer fluid through the absorber tube. The tube-wall heat conduction and the convective and irradiative heat losses to the surroundings were also considered in the model. The average internal and overall heat transfer coefficients were determined for the sinusoidal circumferential non-uniform heat flux distribution span of 160°, 180°, 200° and 240°, and the

360° span of circumferential uniform heat flux for 10 m long absorber tubes of different inner diameters and wall thicknesses with thermal conductivity of 16.27 W/mK between the Reynolds number range of 4 000 and 210 000 based on the inlet temperature. The results showed that the average internal heat transfer coefficients for the 360° span of circumferential uniform heat flux with different concentration ratios on absorber tubes of the same inner diameters, wall thicknesses and thermal conductivity were approximately the same, but the average overall heat transfer coefficient increased with the increase in the concentration ratios of the uniform heat flux incident on the tubes. Also, the average internal heat transfer coefficient for the absorber tube with a 360° span of uniform heat flux was approximately the same as that of the absorber tubes with the sinusoidal circumferential non-uniform heat flux span of 160°, 180°, 200° and 240° for the heat flux of the same concentration ratio, but the average overall heat transfer coefficient for the uniform heat flux case was higher than that of the non-uniform flux distributions. The average axial local internal heat transfer coefficient for the 360° span of uniform heat flux distribution on a 10 m long absorber tube was slightly higher than that of the 160°, 200° and 240° span of non-uniform flux distributions at the Reynolds number of 4 000. The average internal and overall heat transfer coefficients for four absorber tubes of different inner diameters and wall thicknesses and thermal conductivity of 16.27 W/mK with 200° span of circumferential non-uniform flux were found to increase with the decrease in the inner-wall diameter of the absorber tubes. The numerical results showed good agreement with the Nusselt number experimental correlations for fully developed turbulent flow available in the literature.

Key words: absorber tube, solar heat flux, numerical simulation, heat transfer coefficients

Nomenclature

A	surface or cross sectional area, m^2
b_{hf}	heat flux parameters
C_R	concentration ratio of the reflector field
C_μ, C_1, C_2	empirical turbulence constants
c_p	specific heat of the fluid at constant pressure, J/kgK
f	Darcy friction factor
G	kinetic energy transfer
g	acceleration due to gravity, m/s^2
h, \bar{h}	heat transfer coefficient and average heat transfer coefficient, W/m^2K
I	turbulence intensity at inlets and outlets, or number of irradiated divisions
i	irradiated division number
k	thermal conductivity, W/mK
L, L_{TOT}	axial dimension and total axial length of tube, m
M	total number of the axial divisions
\dot{m}	mass flow rate, kg/s
(m, n)	numerical surface location
N	total number of the circumferential divisions
Nu, \overline{Nu}	Nusselt number and average Nusselt number
P	pressure, Pa
Pr	Prandtl number
q	heat transfer, W
q''	heat flux, W/m^2
R, \bar{R}	radius and average radius, m
r	radial coordinate, m

Re	Reynolds number
S	source term
T, \bar{T}	temperature and average temperature, K
t	tube wall thickness, m
U	overall heat transfer coefficient, W/m ² K
v, \bar{v}	velocity and average velocity, m/s
x	axial coordinate, m

Greek Letters

α	angle span of the irradiated segment of the tube, rad
α_{tu}	absorptivity of the absorber tube
ε	turbulent kinetic energy dissipation
ε_{tu}	emissivity of the absorber tube-wall surface
θ	non-uniform temperature factor
γ_{mi}	reflectivity of the concentrator mirrors
κ	turbulent kinetic energy generation
μ	viscosity, kg/ms
ρ	density of the heat transfer fluid, kg/m ³
σ_{SB}	Stefan-Boltzmann constant, W/m ² K ⁴
σ	empirical turbulence constants
φ	conservation variable in governing equations
ϕ	angle span of each circumferential division, °, or tangential dimension
Γ	diffusion coefficient

Subscripts

a	free stream air
b	bulk fluid property
conv	convection
DNI	direct normal irradiation
ed	turbulent eddy
ef	effective
f	fluid
i	inner surface
l	laminar
m	at position m
n	at position n
o	outer surface
r	in radial direction
rad	radiation
x	in axial direction
tu	tube
w	wall
ϕ	in tangential direction
∞	radiant surroundings

1 Introduction

Solar thermal energy is currently one of the most important sources of clean and renewable energy, which has enormous potential in reducing overdependence of the global economy on fossil fuels and in mitigating greenhouse gas emissions. Two basic types of solar thermal collector systems have been developed over the years and they are the non-

concentrating or stationary collectors and the concentrating collectors (Kalogirou, 2004). The non-concentrating collectors, which include flat-plate and evacuated tube collectors, are suitable for low to medium temperature applications. The single-axis sun-tracking concentrating collectors, which include the linear Fresnel collector, parabolic trough collector and cylindrical trough collector types, and the two-axis tracking collectors, such as the parabolic dish reflector and heliostat field collectors, are suitable for medium to high temperature applications as required in the industrial process heat applications and electric power generations.

The parabolic trough solar collector has been the most popular concentrator among other solar concentrating collectors due to the success of the solar electric generating plants in the Mojave Desert of southern California in the late 1980s. The plant size ranges from 30 MW to 80 MW and a total installed capacity of 354 MW_e, which feeds about 800 million kWh per year into the grid and displaces more than 2 million barrels of oil per year (Abbas *et al.* 2012), (Grena2010), (Krothapalli and Greska , nd). Another important linear concentrator, which has received considerable attention for both industrial process heat applications and electric power generation, is the linear Fresnel concentrator (Goswami *et al.* 1990). Unlike parabolic solar collectors, it does not require rotating joints and metal-glass welding at the ends of each receiver tube (Abbas *et al.* 2012) and has low maintenance and operation costs. It also has low construction cost with low wind loads and high ground coverage, which makes it suitable for installation where space is restricted. These features have motivated a number of research efforts to improve the general performance of linear Fresnel solar concentrator systems and construction of solar thermal plants based on the linear Fresnel approach. The first solar thermal power plant based on the linear Fresnel solar concentrator was the 1.4 MW_e installed in Puerto Errado, Spain and a second one being built, with a projected power output of 30 MW_e (Abbas *et al.* 2012a). Also, in the USA, Ausra built a 5

MW_e compact linear Fresnel concentrator demonstration power plant. In 2010, the first linear Fresnel concentrated solar power plant was built in South Africa and now two 150 kW module pilot systems are being constructed at Eskom's (South Africa's largest power utility company) research and innovation centre in Rosherville, Johannesburg (Warwick and Middleton, 2012). The linear Fresnel solar concentrating collector has also been considered as an important option for direct steam generation power plants (Abbas *et al.* 2012). The direct steam generation systems eliminate the need of using the expensive thermo-oil and complex heat exchangers and superheated steam can be generated directly using the concentrating collector. Mills and Morrison (1999) presented the first results from the linear Fresnel solar concentrating collector installation of 1MW_{th} at the Liddell power station completed in 2004. Direct steam generation with the solar array was achieved and optical performance met the design specifications. Also, in the industrial process heat applications, a linear Fresnel concentrating collector can conveniently generate temperatures up to 250 °C or above, but this area of solar thermal technology is almost untouched (Peter, 2008).

The linear Fresnel solar concentrator shown in Fig. 1 consists of arrays of linear mirror strips, which track the sun in a single axis and concentrate the solar radiation on the receiver cavity mounted on the horizontal tower. Each mirror element is tilted such that normally incident solar radiation, after reflection from the mirror element, impinges on the absorber tube placed along the length of the focal zone of the concentrator (Goswami *et al.* 1990). The receiver consists of a compound parabolic cavity with a second-stage concentrator and a single large diameter absorber tube mounted inside the cavity covered with a transparent glass. The second-stage concentrator not only enlarges the target for the Fresnel concentrator but also provides insulation to the absorber tubes (Häberle *et al.* 2002). Another type of linear Fresnel concentrator receiver cavity, which recent studies on solar collector receiver cavity preferred, is the trapezoidal cavity shown in Fig. 2. It consists of multiple absorber tubes

inside the cavity covered with a transparent glass and air trapped inside the cavity. The backsides of the cavity are also covered with opaque insulation to reduce conduction heat losses and the front glass pane to reduce convective heat losses. This also protects the receiver absorber tubes from wind, rain and dirt.

The shortfall of the linear Fresnel solar concentrator is that its concentration factors (10 - 40) are still notably lower than those of parabolic trough concentrators (300 - 1500), but this can be improved with good optical designs (the mirror separation, shape, width and orientation). Also, its thermal performance, which this study focuses on, still requires significant improvement by improving its thermal design models and heat transfer characteristics of its receiver system. Häberle *et al.* (2002) studied the optical performance of the Solarmundo line-focusing Fresnel collector using ray-tracing. The ray-tracing simulation results showed that the radiation intensity was evenly distributed (between 80% and 100% intensity) in the lower part and very low in the upper part of the absorber tube, indicating non-uniform radiation heat flux on the absorber tube. The study also showed that the distribution pattern did not vary significantly for different angles of incident solar radiation. Barale *et al.* (2010) performed optical design of the linear Fresnel collector prototype being built in Sicily, to optimise the geometry of the linear Fresnel collector for the FREeSuN project. The study considered all the relevant optical loss mechanisms - reflector surface errors, tracking errors, shading and blocking due to structure and tracked mirrors, etc. It found that if the receiver was too far from the primary mirror plane, the contribution of errors would drastically reduce the optical performance and that using uniform mirror curvature (one adapted curvature for all mirrors) would prevent the efficient focalisation of all the mirror rows. Pino *et al.* (2012) conducted experimental validation of an optical model of a linear Fresnel collector system using the solar cooling plant with an absorption chiller located in the School of Engineering, University of Seville, Spain. Eck *et al.* (2007) investigated the

thermal load of a direct steam-generating tube with 0.15 m diameter absorber tube located 13 m above a field of 52 primary mirrors of the linear Fresnel collector for a 50 MW solar plant using a finite element method. The study showed that the heat flux distribution was highest at the bottom of the outer surface of the absorber tube followed by the sides and abated contribution came from the top. The studies by Goswami *et al.*(1990) and Mathur *et al.* (1991) also showed that flux distribution on the outer-wall surface of the absorber tube had a peak at the central portion from underneath and decreased rapidly on both sides of the tube. The studies recommended that the unirradiated portion of the absorber tube should be insulated to reduce thermal losses.

The few available studies on thermal performance of the linear Fresnel concentrator receiver absorber tube assumed uniform heat flux distribution on the circumferential outer surface, which is not really so, as revealed in the above studies. Dey (2004) presented the design methodology and thermal modelling of a linear absorber of an inverted receiver cavity for a north-south-oriented compact linear Fresnel reflector. This study assumed uniform solar flux and gave model equations for the absorber tube sizing and spacing, and the possible absorber design configurations. Abbas *et al.* (2012b) carried out a steady-state numerical simulation of the thermal performance of the linear Fresnel collector receiver tubes of the trapezoidal cavity to determine the optimum tube diameter and length. It assumed a uniform radiation flux impinging on the receiver tube. Experimental validation of an optical and thermal model of a linear Fresnel collector by Francisco *et al.* (2011) assumed a uniform radiation flux impinging on the absorber tube. Velázquez *et al.* (2010) carried out a numerical simulation of a linear Fresnel reflector concentrator to evaluate its technical feasibility as a direct generator in a Solar-GAX cycle with a cooling capacity of 10.6 kW. The study also assumed a uniform radiation flux impinging on the receiver and presented one-dimensional

numerical models for the fluid flow inside the receptor tube, heat transfer in the receptor tube wall, heat transfer in cover tube wall, and solar thermal analysis in the solar concentrator.

Numerical studies on the influence of circumferential non-uniform solar heat flux incident on the exterior wall surface of a linear Fresnel collector absorber tube on the heat transfer from the tube outer-wall surface to the heat transfer fluid are lacking in the literature. This study, therefore, numerically investigated the influence of the circumferential non-uniform solar heat flux distribution span of 160° , 180° , 200° and 240° and a 360° uniform heat flux on linear Fresnel collector absorber tubes on the internal and overall heat transfer coefficients between the Reynolds number range of 4 000 and 210 000, based on the inlet temperature. It also compared the influence of circumferential uniform heat flux distribution on the heat transfer coefficients with circumferential non-uniform heat flux, as the actual heat flux distributions on the absorber tubes of a linear Fresnel collector are non-uniform and previous studies were based on uniform heat flux or isothermal wall temperature. The three-dimensional steady-state numerical simulations are implemented based on ANSYS Fluent code version 14. The non-uniform solar heat flux distribution on the outer wall of the absorber tube is modelled as a first order approximation as a sinusoidal function of the radiation heat flux incident on the circumference of the absorber tube. The tube-wall heat conduction and the convective and irradiative heat losses to the surroundings were considered in the model. The convective heat flux loss due to wind effect around the receiver and the radiative heat flux loss constitute the dominant thermal losses that influence thermal performance of the receiver absorber tubes of solar thermal concentrating collectors in the actual operation conditions, and were modelled using first-order approximations. Also, important simplifications of the model domain were made in order to focus the study on the heat flux distributions on the tubes by neglecting the possible heat conduction through the insulated sidewalls and the glass cover of the receiver cavity. A single absorber tube was

selected, since the tubes are the same and assumed to be exposed to its surrounding, while receiving the solar heat flux from underneath. The k- ϵ model was employed to simulate the turbulent flow of a heat transfer fluid through the absorber tube. The internal and overall heat transfer coefficients for four absorber tubes of 10 m long with different inner-wall diameters and thicknesses modelled with 200° span of sinusoidal circumferential non-uniform heat flux at the considered Reynolds number range were also obtained from the simulation results.

2. Physical model description

The concentrated solar heat flux, which impinges on the outer-wall surface of the absorber tube of a linear Fresnel concentrating collector from underneath, results in non-uniform heat flux distribution on the circumferential surface of the tube. The non-uniform heat flux results in a non-uniform wall temperature profile around the tube wall and hence non-uniform heat transfer to the heat transfer fluid in the tube. Fig. 3 shows a single absorber tube model of a trapezoidal receiver cavity of a linear Fresnel concentrating collector divided into $M \times N$ number of numerical surfaces. The tube consists of wall thickness t , inner radius, R_i , outer radius R_o and total length of the tube L_{TOT} .

Fig. 4 shows the cross-section of the absorber tube irradiated with concentrated solar heat flux from the bottom segments. The numbering system for simulating the variation of circumferential heat flux distribution on the tube is also given. The angle span of the unirradiated segment in radians is $2\pi - \alpha$ and α is the angle span of the irradiated segment of the tube. The circumferential surface of the tube is divided into N segments and each of the segments subtends an angle span of ϕ defined as:

$$\phi = \frac{2\pi}{N} \quad (1)$$

where N is the total number of the circumferential segments. In this study, N equal to 36 was considered. $n_{i=1}$ is the segment (in a clockwise fashion) where irradiation starts and can be expressed in terms of α .

$$n_{i=1} = \frac{[N - (\alpha/2\pi) \times N]}{2} + 1 \quad (2)$$

with $n = 1, 2, 3 \dots N = 36$, $i = 1, 2, 3 \dots I$, where I is the number of segments that are directly irradiated (with α being multiples of 20°):

$$I = \frac{\alpha}{2\pi} N \quad (3)$$

3. Mathematical formulation

The numerical heat transfer model developed in this study considered the concentrated circumferential solar heat flux impinging on the outer-wall surface of linear Fresnel concentrating collector absorber tubes, the heat transferred to the fluid, conductive heat transfer in the absorber tube wall (radially, axially and tangentially) and the heat flux losses to the surroundings (via convection and radiation).

3.1 Numerical heat transfer model

Fig. 5 shows the heat transfer components on the control volume (CV) of an element at location (m, n) on the absorber tube model in Fig. 3, with the following dimensions in the (r, ϕ, x) coordinate system: t , ϕ , and L respectively. A_o and A_i are the outer- and inner-wall surface areas defined in equations (4) and (5), while A_x and A_ϕ are the axial and tangential direction surface areas defined in eqns. (6) and (7).

$$A_o = L \cdot \phi \cdot R_o \quad (4)$$

$$A_i = L \cdot \phi \cdot R_i \quad (5)$$

$$A_x = \frac{1}{2} t (R_o + R_i) \quad (6)$$

$$A_\phi = L \cdot t \quad (7)$$

By applying an energy balance on the element, the heat transfer model under steady-state condition is obtained as follows:

$$q_{o,(m,n)} = q_{i,(m,n)} + q_{x,(m,n)} + q_{x,(m+1,n)} + q_{\phi,(m,n)} + q_{\phi,(m,n+1)} + q_{o,conv,(m,n)} + q_{o,rad,(m,n)} \quad (8)$$

Each term are briefly discussed in the following text.

$q_{o,(m,n)}$ is the concentrated solar heat transfer on the outer wall surface at location (m, n) expressed as follows:

$$q_{o,(m,n)} = q_{o,(m,n)}'' A_o \quad (9)$$

$q_{o,(m,n)}''$ is the solar heat flux reflected by the linear Fresnel concentrator mirror field on the absorber tube at (m, n) . If the location (m, n) is at the un-irradiated segment of the tube, then $q_{o,(m,n)}''$ was assumed to be zero for purposes of this study. $q_{i,(m,n)}$ is the heat transferred to the working fluid at location (m, n) , which can be expressed as follows:

$$q_{i,(m,n)} = h_{i,(m,n)} \cdot A_i (T_{w,i,(m,n)} - T_{b,m}) \quad (10)$$

where $h_{i,(m,n)}$ is the local internal convective heat transfer coefficient, $T_{w,i,(m,n)}$ is the local inner-wall temperature and $T_{b,m}$ is the fluid bulk temperature at the axial position m defined as:

$$T_{b,m} = T_{b,m-1} + \frac{\sum_{n=1}^N q_{i,(m,n)}}{\dot{m} c_p} \quad (11)$$

where $q_{i,(m,n)}$ is the average inner-wall heat transfer, \dot{m} is the mass flow rate of the heat transfer fluid and c_P is the specific heat of the heat transfer fluid. $q_{x,(m,n)}$ and $q_{x,(m+1,n)}$ are the conductive heat transfers in the axial direction modelled from Fourier's law of heat conduction (Cengel, 2007) as follows:

$$q_{x,(m,n)} = \frac{k_{tu} A_x}{L} (\bar{T}_{tu,(m,n)} - \bar{T}_{tu,(m-1,n)}) \quad (12)$$

$$q_{x,(m+1,n)} = \frac{k_{tu} A_x}{L} (\bar{T}_{tu,(m,n)} - \bar{T}_{tu,(m+1,n)}) \quad (13)$$

where \bar{T}_{tu} is the average tube material temperature of the element.

The conductive heat transfers in the tangential direction, $q_{\phi,(m,n)}$ and $q_{\phi,(m,n+1)}$ are also modelled with the Fourier law as follows with \bar{R} being the average tube wall radius:

$$q_{\phi,(m,n)} = \frac{k_{tu} A_{\phi}}{\bar{R} \phi} (\bar{T}_{tu,(m,n)} - \bar{T}_{tu,(m,n-1)}) \quad (14)$$

$$q_{\phi,(m,n+1)} = \frac{k_{tu} A_{\phi}}{\bar{R} \phi} (\bar{T}_{tu,(m,n)} - \bar{T}_{tu,(m,n+1)}) \quad (15)$$

$q_{o,conv,(m,n)}$ is the convective heat transfer loss from the outer-wall surface at (m, n) to the surroundings due to wind effect around the absorber tube modeled from Newton's law of cooling (Rajput, 2005) as:

$$q_{o,conv} = h_{o,(m,n)} \cdot A_o (T_{w,o,(m,n)} - T_a) \quad (16)$$

where $T_{w,o,(m,n)}$ is the outer-wall temperature at (m, n) , T_a is the ambient free stream air temperature and $h_{o,(m,n)}$ is the external convective heat transfer coefficient (Tiwari, 2006) related to the wind velocity, v_a [m/s] around the tube:

$$h_{o,(m,n)} = \bar{h}_o = 5.7 + 3.8v \quad (17)$$

$v_a = 4.36$ m/s was used in this study. $q_{o,rad,(m,n)}$ is the radiative heat transfer loss to the surroundings modelled from the Stefan-Boltzmann law of the emissive power of a surface at a thermodynamic temperature as follows:

$$q_{o,rad,(m,n)} = \varepsilon_{tu} \sigma_{SB} A_o (T_{w,o,(m,n)}^4 - T_\infty^4) \quad (18)$$

where ε_{tu} is emissivity of the absorber tube surface and σ_{SB} is the Stefan-Boltzmann constant (5.67×10^{-8} W/m² · K⁴) (Cengel, 2007) and T_∞ is the radiant temperature of the surrounding.

From equation (10), the local internal convective heat transfer coefficient, $h_{i,(m,n)}$ is related to the local Nusselt number as follows:

$$Nu_{i,(m,n)} = \frac{h_{i,(m,n)} 2R_i}{k_f} = \frac{q_{i,(m,n)}}{\pi L k_f [T_{w,i,(m,n)} - T_{b,m}]} \quad (19)$$

where k_f is the thermal conductivity of the heat transfer fluid assumed to be independent of temperature. The circumferential average Nusselt number of the tube model, which is usually of more practical interest than the local Nusselt number of the tube, is expressed as follows:

$$\overline{Nu}_{i,m} = \frac{\overline{h}_{i,m} 2R_i}{k_f} \quad (20)$$

where $\overline{h}_{i,m}$ is the circumferential average internal heat transfer coefficient:

$$\overline{h}_{i,m} = \frac{\sum_{n=1}^N q_{i,(m,n)}}{2\pi R_i L (\overline{T}_{w,i,m} - T_{b,m})} \quad (21)$$

and where $\overline{T}_{w,i,m}$ is the circumferential average local inner-wall temperature

$$\overline{T}_{w,i,m} = \frac{1}{N} \sum_{n=1}^N T_{w,i,(m,n)} \quad (22)$$

Another useful value is the average internal heat transfer coefficient on the inner wall over the full length of the tube \overline{h}_i in terms of the overall inner wall surface temperature, $\overline{T}_{w,i}$:

$$\bar{h}_i = \frac{\sum_{m=1}^M \sum_{n=1}^N q_{i,(m,n)}}{2\pi R_i L_{TOT} (\bar{T}_{w,i} - \bar{T}_b)} \quad (23)$$

With this the average Nusselt number, \overline{Nu}_i , and overall heat transfer coefficient, U , from the absorber tube surroundings to the heat transfer fluid in the tube can be determined as expressed by Duffie and Beckman (1980):

$$U = \left[\frac{1}{U_o} + \frac{R_o}{\bar{h}_i R_i} + \frac{R_o}{k_{tu}} \ln\left(\frac{R_o}{R_i}\right) \right]^{-1} \quad (24)$$

Here U_o is the overall heat loss coefficient due to convective and radiative heat flux losses from the external surface of the tube. When $T_a = T_\infty$ (as are assumed in this paper for simplicity reasons), this can be written as:

$$U_o = \bar{h}_{rad} + \bar{h}_o \quad (25)$$

where \bar{h}_o is the forced convective heat transfer coefficient due to wind defined in eqn. (17) and \bar{h}_{rad} is the average equivalent radiation heat transfer coefficient from the outer-wall surface of the tube to the surrounding expressed as:

$$\bar{h}_{rad} = \varepsilon_{tu} \sigma_{SB} (\bar{T}_{w,o} + T_\infty) (\bar{T}_{w,o}^2 + T_\infty^2) \quad (26)$$

To determine $\bar{h}_{i,m}$ and \bar{h}_i numerical simulations were performed at different mass flow rate and heat flux distribution cases in ANSYS Fluent version 14.0. A surrounding temperature of 303 K was used in all results.

(i) Circumferential uniform heat flux transfer

In a case where the exterior wall of the tube is exposed to uniform heat flux, the concentrated solar heat transfer $q_{o,(m,n)}$ in eqn. (8) is considered constant over the circumferential outer-wall surface of the absorber tube. Therefore, the concentrated uniform heat transfer over the circumferential outer-wall surface of the tube model in Fig. 3 is implemented as follows:

$$q''_{o,(m,n)} = q''_{DNI} \times b_{hf} \times A_o \quad (27)$$

where $m = 1, 2, 3 \dots M$ and $n = 1, 2, 3 \dots N$ and q''_{DNI} is the direct normal irradiation heat flux concentrated on the circumferential outer-wall surface of the tube model and b_{hf} is the parameter of the concentrating collector defined as:

$$b_{hf} = \varepsilon_{tu} \alpha_{tu} \gamma_{mi} C_R \quad (28)$$

where α_{tu} is the absorptivity and ε_{tu} is the emissivity of the tube-wall surface, γ_{mi} is the reflectivity of the concentrator mirrors and C_R is the concentration ratio of the mirror reflector field (Mathur *et al.* 1991). This study assumed that the linear Fresnel concentrating collector has a tracking system to follow the sun, the reflector mirrors are specularly reflecting and the radiation is normally incident on the concentrator mirrors. The optical efficiency of the concentrator and the reflectivity of the mirrors were assumed to be 100% for purposes of this study.

(ii) Circumferential non-uniform heat flux

In a non-uniform heat flux case, the heat transfer on the irradiated segment of the absorber tube is such that the lower central portions of the irradiated segment ($n = 18$ and $n = 19$, in Fig. 4) receive the highest intensity level of the solar heat flux, which decreases upwards on both sides of the tube to the unirradiated top segment. The concentrated solar heat flux on the irradiated segment was implemented in this study as a sinusoidal function of the direct normal irradiation heat flux (q''_{DNI}) as follows:

$$q''_{o,(m,n)} = q''_{DNI} \sin \left[\frac{\pi}{\alpha} \left(n - n_{i=1} + \frac{1}{2} \right) \right]$$

$$q''_{o,(m,n)} = 0, \quad \text{if } n < n_{i=1} \quad (29)$$

$$q''_{o,(m,n)} = 0, \quad \text{if } n \geq n_{i=1} + I$$

where $m = 1, 2, 3 \dots M$, $n = 1, 2, 3 \dots N$ and $i = 1, 2, 3 \dots I$ The sinusoidal function of the heat flux in eqn. (29) gave an average intensity level of 97% of the radiation heat flux distributions at the lower bottom portion of the tube model, which then decreased down to the unirradiated upper portion of the tube, while in Häberle *et al.* (2002), the solar flux radiation distributions was between 80% and 100% at the bottom lower part and very low in the upper part of the absorber tube. Also in Eck *et al.* (2007), the proportion of heat flux distribution was maximum at the bottom of the outer surface of the absorber tube followed by the sides and then decreased to the top portion of the tube.

3.2 Fluid flow through the absorber tube model

The fluid flow through the absorber tube model in Fig. 3 is assumed incompressible, steady-state and fully developed turbulent flow. The governing equations for the fluid flow through the tube are the continuity, momentum and energy equations and the k-ε two-equation turbulent model equations (Yildiz *et al.* 2006), (Vikram *et al.* 2010), (Mehmet and Tiirkan, 1997). These governing equations in cylindrical coordinates (r, ϕ, x) are expressed as follows:

Continuity equation:

$$\frac{1}{r} \frac{\partial(rv_r)}{\partial r} + \frac{1}{r} \frac{\partial v_\phi}{\partial \phi} + \frac{\partial v_x}{\partial x} = 0 \quad (30)$$

where v_r, v_ϕ and v_x are the radial, polar and axial velocity components respectively.

Momentum equations:

r -momentum:

$$\rho \left(v_r \frac{\partial v_r}{\partial r} + \frac{v_\phi}{r} \frac{\partial v_r}{\partial \phi} + v_x \frac{\partial v_r}{\partial x} - \frac{v_\phi^2}{r} \right) = -\frac{\partial p}{\partial r} + \mu_{ef} \left[\nabla^2 v_r - \frac{v_r}{r^2} - \frac{2}{r^2} \frac{\partial v_\phi}{\partial \phi} \right] + \rho g_r \quad (31)$$

ϕ -momentum:

$$\rho \left(v_r \frac{\partial v_\phi}{\partial r} + \frac{v_\phi}{r} \frac{\partial v_\phi}{\partial \phi} + v_x \frac{\partial v_\phi}{\partial x} - \frac{v_r v_\phi}{r} \right) = -\frac{1}{r} \frac{\partial p}{\partial \phi} + \mu_{ef} \left[\nabla^2 v_\phi - \frac{v_\phi}{r^2} + \frac{2}{r^2} \frac{\partial v_r}{\partial \phi} \right] + \rho g_\phi \quad (32)$$

x -momentum:

$$\rho \left(v_r \frac{\partial v_x}{\partial r} + \frac{v_\phi}{r} \frac{\partial v_x}{\partial \phi} + v_x \frac{\partial v_x}{\partial x} \right) = -\frac{\partial p}{\partial x} + \mu_{ef} \nabla^2 v_x + \rho g_x \quad (33)$$

where $\nabla^2 \equiv \frac{1}{r} \frac{\partial}{\partial r} \left(r \frac{\partial}{\partial r} \right) + \frac{1}{r^2} \frac{\partial^2}{\partial \phi^2} + \frac{\partial^2}{\partial x^2}$ and μ_{ef} is the total effective viscosity of the

flow defined as:

$$\mu_{ef} = \mu_l + \mu_{ed} \quad (34)$$

μ_l is the laminar viscosity and μ_{ed} is the turbulent eddy viscosity defined as:

$$\mu_{ed} = \rho C_\mu \frac{\kappa^2}{\varepsilon} \quad (35)$$

Here C_μ is an empirical turbulent constants and ε is the turbulent energy dissipation.

Energy equation:

$$\frac{1}{r} \frac{\partial}{\partial r} (\rho r v_r T) + \frac{1}{r} \frac{\partial}{\partial \phi} (\rho v_\phi T) + \frac{\partial}{\partial x} (\rho v_x T) = \frac{1}{r} \frac{\partial}{\partial r} \left(r \left(\mu_l + \frac{\mu_{ed}}{\sigma_{ed}} \right) \frac{\partial T}{\partial r} \right) + \quad (36)$$

$$\frac{1}{r} \frac{\partial}{\partial \phi} \left(\frac{1}{r} \left(\mu_l + \frac{\mu_{ed}}{\sigma_{ed}} \right) \frac{\partial T}{\partial \phi} \right) + \frac{\partial}{\partial x} \left(\left(\mu_l + \frac{\mu_{ed}}{\sigma_{ed}} \right) \frac{\partial T}{\partial x} \right)$$

Turbulence model equation:

The turbulent flow of the heat transfer fluid in the absorber tube model is modelled using the k - ε two-equation turbulence model obtained from the Navier-Stokes equation (Yildiz *et al.* 2006). The k - ε two-equation turbulence model is expressed as follows:

k-equation turbulence model

$$\begin{aligned} \frac{1}{r} \frac{\partial}{\partial r} (\rho r v_r \kappa) + \frac{1}{r} \frac{\partial}{\partial \phi} (\rho v_\phi \kappa) + \frac{\partial}{\partial x} (\rho v_x \kappa) &= \frac{1}{r} \frac{\partial}{\partial r} \left(r \left(\mu_l + \frac{\mu_{ed}}{\sigma_\kappa} \right) \frac{\partial \kappa}{\partial r} \right) + \\ & \frac{1}{r} \frac{\partial}{\partial \phi} \left(\frac{1}{r} \left(\mu_l + \frac{\mu_{ed}}{\sigma_\kappa} \right) \frac{\partial \kappa}{\partial \phi} \right) + \frac{\partial}{\partial x} \left(\left(\mu_l + \frac{\mu_{ed}}{\sigma_\kappa} \right) \frac{\partial \kappa}{\partial x} \right) + G - \rho \varepsilon \end{aligned} \quad (37)$$

ε -equation turbulence model

$$\begin{aligned} \frac{1}{r} \frac{\partial}{\partial r} (\rho r v_r \varepsilon) + \frac{1}{r} \frac{\partial}{\partial \phi} (\rho v_\phi \varepsilon) + \frac{\partial}{\partial x} (\rho v_x \varepsilon) &= \frac{1}{r} \frac{\partial}{\partial r} \left(r \left(\mu_l + \frac{\mu_{ed}}{\sigma_\varepsilon} \right) \frac{\partial \varepsilon}{\partial r} \right) + \\ & \frac{1}{r} \frac{\partial}{\partial \phi} \left(\frac{1}{r} \left(\mu_l + \frac{\mu_{ed}}{\sigma_\varepsilon} \right) \frac{\partial \varepsilon}{\partial \phi} \right) + \frac{\partial}{\partial x} \left(\left(\mu_l + \frac{\mu_{ed}}{\sigma_\varepsilon} \right) \frac{\partial \varepsilon}{\partial x} \right) + \frac{\varepsilon}{\kappa} (GC_1 - C_2 \rho \varepsilon) \end{aligned} \quad (38)$$

Where C_μ , C_1 , C_2 , σ_κ , σ_ε and σ_{ed} are the empirical turbulent constants in eqns. (31) to (38) given as $C_\mu = 0.09$, $C_1 = 1.43$, $C_2 = 1.92$, $\sigma_\kappa = 1.0$, $\sigma_\varepsilon = 1.3$ and $\sigma_{ed} = 0.9$. The production term, G , represents the kinetic energy transfer from the mean flow to the turbulent motion through the interaction between the turbulent fluctuations and the mean flow velocity gradients (Vikram *et al.* 2010). The equations (30) to (38) are reduced to convection-diffusion general equations in cylindrical coordinates in eqn. (39) and then solved numerically.

$$\begin{aligned} \frac{1}{r} \frac{\partial (\rho r v_r \varphi)}{\partial r} + \frac{1}{r} \frac{\partial (\rho v_\phi \varphi)}{\partial \phi} + \frac{\partial (\rho v_x \varphi)}{\partial x} &= \Gamma_\varphi \nabla^2 \varphi + S_\varphi \\ &= \Gamma_\varphi \left[\frac{1}{r} \frac{\partial}{\partial r} \left(r \frac{\partial \varphi}{\partial r} \right) + \frac{1}{r^2} \frac{\partial^2 \varphi}{\partial \phi^2} + \frac{\partial^2 \varphi}{\partial x^2} \right] + S_\varphi \end{aligned} \quad (39)$$

The diffusion coefficient, Γ_ϕ , corresponding to the conservation variable ϕ (i.e. mass, momentum and energy conservations) and the source term S_ϕ are presented in Table 1.

3.3 Boundary conditions

The boundary conditions for the absorber tube model with uniform heat flux and non-uniform heat flux are specified as follows:

Inlet boundary conditions ($x = 0$):

The mass flow inlet boundary condition is specified as:

$$\dot{m}_r = \dot{m}_\phi = 0 \text{ kg/s} \quad \text{and} \quad \dot{m}_x = \text{uniform} \quad (40)$$

Fluid inlet temperature:

$$T_f(\phi, r) = T_{b,0} = 300 \text{ K} \quad (41)$$

The turbulence variables at the inlet and outlet of the absorber tube are specified using an empirical relation for the turbulence intensity I (ANSYS Fluent version 14.0, 2011):

$$I \equiv \frac{\sqrt{\frac{2}{3}k}}{\bar{v}_{avg}} \cong \frac{0.16}{\text{Re}^{\frac{1}{8}}} \quad (42)$$

With the fluid Reynolds number based on bulk fluid properties defined as:

$$\text{Re} = \frac{2\rho_b \bar{v}_x R_i}{\mu_b} \quad (43)$$

Outlet boundary conditions ($x = L_{TOT}$):

The pressure outlet-type boundary condition is specified as:

$$P(\phi, r) = P_o \quad (44)$$

Absorber tube inner-wall surface boundary condition ($r = R_i$):

No-slip conditions are applied at inside wall surface of the absorber tube:

$$v_r = v_\phi = v_x = 0 \quad (45)$$

External wall surface boundary conditions ($r = R_o$):

A heat flux boundary condition was employed onto outer-wall surface boundary by using a user-defined function in FLUENT.

$$\dot{q}''_{(m,n)} = \dot{q}''_{o,(m,n)} + U_o (T_{w,o,(m,n)} - T_\infty) \quad (46)$$

Near-wall flow boundary condition:

The k- ϵ two-equation turbulence model cannot be applied in the regions close to solid walls where viscous effects are dominant over turbulence (Cheng *et al.* 2012). The two methods normally employed in solving the near-wall region flow problems are the low Reynolds number modelling and wall function method. The standard wall function in FLUENT (ANSYS Fluent version 14.0, 2011) was adopted in solving the near-wall region flow in the absorber tube inner wall.

4. Numerical procedure, grid analysis and code validation

The governing equations in eqns. (30) – (39) were solved numerically with the finite volume method described well by Patankar (1980), Ferziger and Perifi (2002) and Versteeg and Malalasekera (1995). The computational domain, which consists of the absorber tube and the heat transfer fluid flowing through the tube, was meshed with Hex8 and Wed6 grid structures. The convective terms in the momentum and energy equations were discretised with the second-order upwind scheme and the standard SIMPLEC algorithm was used for the pressure-velocity coupling. The convergence criteria for the continuity and momentum equations and the energy equation were when the maximum residual were less than 10^{-5} and 10^{-7} respectively.

Mesh dependence was also checked in terms of the temperature rise of the fluid. The mesh were refined by increasing the mesh density until further refinement did not result in any significant change in the outlet temperature of the fluid. Energy balance checks were also performed of the heat transfer model, which gave an average percentage error of < 1% of the

resultant incident heat flux on the tube. The grid refinement test results at a Reynolds number of approximately 12 000 for uniform heat flux, q_o'' are presented in Table 2. The geometry of the absorber tubes and the thermophysical properties of the heat transfer fluid and the solar heat flux and concentrating collector parameters used in the numerical study are presented in Tables 3, 4 and 5.

The absorber tube diameters were selected based on the internal pressure restrictions on tubes and pipes by the Austrian Boiler Standard, considering maximum operating temperature of 350 °C and the corresponding saturation pressure of 16.62 MPa (OneSteel Building Services, 2003). The thermal properties of the heat transfer fluid and the absorber tube material are assumed to be constant. The beam solar irradiation heat flux in Table 5 was generated using the solar calculator of the solar load model built in the FLUENT code. The beam solar irradiation calculated with the solar calculator in Pretoria, South Africa, with -25° longitude, 28° latitude and GMT +2 on the selected day, 21 July at 13:00 pm under fair-weather conditions is 787.263W/m², which was considered as the period of the year with lower solar heat flux. Table 5 contains information on the three heat flux intensity levels that will be considered that results from the concentration ratios: $C_R = 10$, $C_R = 20$, and $C_R = 30$.

The validation of the numerical model was carried out by comparing the Nusselt number, \overline{Nu}_i , determined from the simulation results with the standard empirical correlations of the Nusselt number in terms of the friction factor, f , Reynolds number, Re , and Prandtl number, Pr , for fully developed turbulent flow in circular tubes presented in Table 6. The Gnielinski experimental correlation is considered to give the most accurate results (Cengel, 2007). The Petukhov correlations also give accurate results, but better than the Sieder and Tate correlation.

Fig. 6 shows the Nusselt number \overline{Nu}_i obtained from the ANSYS Fluent numerical results and that obtained from the standard empirical correlations in Table 6 in the Reynolds number

range of 4 000 to 210 000 for a 10 m long absorber tube modelled with a 360° span of circumferential uniform solar heat flux distribution with $q_o'' = 7.1 \text{ kW/m}^2$ ($C_R = 10$). The tube consists of an inner diameter of 62.7 mm, wall thickness of 5.16 mm and tube thermal conductivity of 16.27 W/mK. It was found that the Nusselt number obtained from the numerical model is generally in good agreement with the experimental correlations and gave average deviations of 5.2% in terms of the Gnielinski correlations, 5.5% in terms of the Petukhov correlations and 11.3% in terms of the Sieder and Tate correlation.

5. Results and discussion

5.1 Temperature contours of the uniform and non-uniform heat flux distributions

Fig. 7 shows the temperature contours of the circumferential uniform heat flux and the sinusoidal circumferential non-uniform heat flux distributions of the heat flux in table 5 with $C_R = 10$ on the outer-wall surface of the 10 m long absorber tubes subject to convective heat flux loss due to wind effect and radiative heat flux loss to the surroundings. The heat transfer fluid flows through absorber tubes are in the x -axial direction, as indicated by the arrows in Fig. 7. The temperature contours for the $\alpha = 360^\circ$ span of uniform heat flux distribution indicated that the outer-wall temperature of the tube increased in the fluid flow direction and was greater at the outlet of the tube. The temperature contours for the spans with $\alpha = 160^\circ$, 180° , 200° and 240° of non-uniform heat flux distribution cases indicated non-uniform circumferential temperature profiles on the outer-wall surface of the tubes, which increased in the fluid flow direction and decreased tangentially from the irradiated bottom portion to the unirradiated top portion of the tubes. The contours also showed that the circumferential outer-wall temperature of the tubes was greater at the outlet of the tubes and increased with the increase in angle span of the heat flux distributions on the outer-wall surface of the tubes. The blue colour indicator at the unirradiated top portion of the tube inlet shows that the fluid

layers at that portion were unheated, while the bottom portion of the tube outlet was the most heated portion of the tubes as indicated by the red hot colour.

The non-uniformity of the temperatures obtained for the input values mentioned above are also demonstrated in Figure 8, where the non-uniform temperature factor, θ , given in equation (47) is plotted against the circumferential position for different α values.

$$\theta = \frac{\bar{T}_{w,o,(n)} - T_{b,(m=0)}}{\bar{T}_{w,o,uniform} - T_{b,(m=0)}} \quad (47)$$

Here $\bar{T}_{w,o,(n)}$ refers to the average axial temperature for segment n , $T_{b,(m=0)}$ refers to the inlet bulk fluid temperature of the tube and $\bar{T}_{w,o,uniform}$ refers to the average overall wall temperature obtained when a uniform heat flux is applied. If θ is less than 1, it indicates that the wall temperature at location n is colder than what it would have been if a uniform heat flux was applied. If θ is zero, it indicates that the wall temperature is equal to the inlet bulk fluid temperature. From Figure 8 it can be seen that for all non-uniform heat flux cases, all tube locations were colder than with a uniform heat flux case. The peak portion of the profile corresponds to the lower central portion of the tubes with the maximum incident heat flux, where the fluid in the tube was mostly heated. It also shows that at the two ends of the profiles, the outer-wall to inner-wall surface temperature factor was very low, indicating that very little amount of heat was conducted to the un-irradiated top portion of the tube, where the fluid was least heated.

5.2 External wall surface uniform and non-uniform heat flux distribution contours

Fig. 9 shows the total surface heat flux contours of the circumferential uniform heat flux and those of the sinusoidal circumferential non-uniform heat flux distributions on the external wall surfaces of the tubes in Fig. 7. For the 360° span of uniform heat flux, the contour showed uniform surface heat flux over the circumferential surface of the tube. For the 160°, 180°, 200° and 240° spans of non-uniform heat flux, the contours showed that the total

surface heat flux decreased from the bottom central portion, which received the highest proportion of the concentrated incident solar heat flux to the unirradiated top portion of the tubes. Also, for the non-uniform heat flux cases, the contours showed that the total surface heat flux increased with the increase in the angle span of the incident heat flux distributions and that the heat flux was conducted tangentially to the unirradiated top portion of the tubes. The total heat transfer at the outer wall of the absorber tubes varied between the uniform and various non-uniform heat flux distribution cases considered. The non-uniform heat flux cases were based on the sinusoidal function of the considered heat flux, while the uniform heat flux cases were based on the uniform distribution of the heat flux around the tubes.

5.3 Sinusoidal circumferential non-uniform heat flux distribution profiles

Fig. 10 shows the sinusoidal circumferential heat flux distribution profiles of the 160°, 180°, 200°, 220° and 240° span of the heat flux in Table 5 with $C_R = 10$ on the outer-wall surface of the absorber tube model based on equation (29) and the numbering system described in Fig. 4. The Fig.10 shows that the peak portion of the radiation intensity profile is where $n = 18$ and 19, which corresponds to the lower central portion of the tube. The two horizontal ends of the profile which has lower radiation intensities refer to the unirradiated portions of the tube. The sinusoidal heat flux distribution profile is similar to that of ray-tracing simulation results reported by (Häberle *et al.* 2002) on the optical performance of the Solarmundo line-focusing Fresnel collector using ray-tracing. The ray-tracing results showed that the solar flux radiation was evenly distributed (between 80% and 100%) at the bottom lower part and very low in the upper part of the absorber tube. This result is similar to that of sinusoidal heat flux distributions, which gave an average intensity level of 97% of the radiation heat flux distributions at the lower bottom portion of the tube, indicating where the tube received the maximum proportion of heat flux as shown in Fig. 10, and then decreased down to the unirradiated upper portion of the tube.

Fig. 11 shows the circumferential inner-wall heat flux distribution profiles for five external circumferential non-uniform heat flux distributions with spans of 160° , 180° , 200° , 220° and 240° based on the sinusoidal function of the heat flux given in Fig 10. It shows that the circumferential inner-wall heat flux value increased as the angle span of the heat flux distribution increased. It also shows that the circumferential inner-wall heat flux distribution was greatest at the peak portion of the profile. This portion corresponds to the lower central portion of the tube, which received the highest proportion of the incident-concentrated solar heat flux and the highest heat transfer rate to the fluid. Even though the tangential heat conduction in the tube wall resulted in the increase in the inner-wall surface heat flux at the unirradiated upper portion of the tube, the heat transfer to the fluid in these regions was still significantly smaller than at the lower portion of the tube.

5.4 Heat transfer coefficients for the absorber tube with uniform heat flux distributions

Fig. 12 presents the variation of the average internal heat transfer coefficient with the Reynolds number for three absorber tubes of 10 m long with the same inner diameter of 62.7 mm, wall thickness of 5.16 mm and thermal conductivity of 16.27 W/mK. The absorber tubes were modelled with a 360° span of circumferential uniform heat flux distributions of 7.1 kW/m^2 , 14.2 kW/m^2 and 21.3 kW/m^2 respectively. The heat fluxes were obtained by increasing the concentration ratio, C_R from 10 to 20 and 30, thereby increasing the incident heat flux on the absorber tubes. It was found that the average internal heat transfer coefficients of the tubes increased with the Reynolds number due to the decrease in the inner-wall-to-fluid bulk temperature difference with the Reynolds number as shown in Fig. 13. Also, the increase in the irradiation heat flux incident on the absorber tubes by increasing the concentration ratio of the heat flux did not result in any significant increase in the average internal heat transfer coefficient of the tubes. This shows that the average internal heat transfer coefficient was not affected by increasing the concentration ratio of the external wall

uniform heat flux distribution. Thus, Fig. 12 demonstrated that increasing the uniform radiation heat flux incident on the absorber tube of the same geometry and thermal conductivity and the fluid flow at same Reynolds number does not result in any significant increase in the internal heat transfer coefficient. This can be attributed to insignificant secondary flow influences in the turbulent flow regime.

Fig. 14 shows the variations of the outlet temperature of the heat transfer fluid of the absorber tubes with the heat flux of 7.1 kW/m^2 , 14.2 kW/m^2 and 21.3 kW/m^2 presented in Fig. 12. It shows that the outlet temperature of the heat transfer fluid for the absorber tubes considered increased with the increase in heat flux due to the increase in heat transfer rate to the fluid. Energy balance checks of the heat transfer model were performed. As expected from the energy balance principle, the temperature increase in the heat transfer fluid (difference between the outlet and inlet temperatures) with the heat flux of 14.2 kW/m^2 was approximately twice the temperature raise for the 7.1 kW/m^2 case (the exact factor is very dependent on the overall thermal efficiency of the tube). Similarly, the temperature raise for the 21.2 kW/m^2 case was approximately three times that of the 7.1 kW/m^2 case for all mass flow rates. As expected it was also found that the outlet temperatures of the heat transfer fluid decreased with increased mass flow rates.

Fig. 15 presents the variations of the average overall heat transfer coefficients determined from equation (24), with increase in Reynolds number. It was found that the average overall heat transfer coefficient increased with the increase in Reynolds number and that it was approximately the same at higher Reynolds number. This indicated that the average overall heat transfer coefficient had reached the maximum value and that the heat transfer processes from the outer-wall surface of the absorber tubes to the heat transfer fluid no longer changed significantly with the increase in Reynolds number for the absorber tubes and heat flux cases

considered. The average percentage difference for the average overall heat transfer coefficient of the uniform heat flux with $C_R = 30$ was 1.7% higher than that of $C_R = 10$ and 0.9% higher than that of $C_R = 20$. Since each C_R case had approximately the same \bar{h}_i with the increase in Reynolds number as shown in Fig. 12, the increase in the average overall heat transfer coefficient as shown in Fig. 15 could be due to the increase in the overall heat loss coefficient component of the eqn. (25), which depended on the convective and radiative loss coefficients of the tubes. This is especially true since the radiative heat transfer coefficient does not scale linearly.

5.5 Heat transfer coefficient for the absorber tube with different heat flux distributions

Fig. 16 shows the variation of the average internal heat transfer coefficient with the Reynolds number for five circumferential heat flux distribution cases considered. For the 360° span case, circumferential uniform heat flux with $C_R = 10$ was used, while the sinusoidal function of the heat flux with $C_R = 10$ was also used for the case of the 160°, 180°, 200° and 240° span of circumferential non-uniform heat flux respectively. The average internal heat transfer coefficients for the circumferential uniform heat flux and non-uniform heat flux distributions increased with the increase in Reynolds number due to the decrease in the inner-wall-to-fluid bulk temperature difference and the heat flux losses. The decrease in heat flux losses with the increase in Reynolds number was due to the decrease in the outer-wall temperature of the tubes as result of the increase in the internal heat transfer coefficient resulting from the increase in the turbulent mixing of the heat transfer fluid with the increase in Reynolds number. The average internal heat transfer coefficient for the absorber tube modelled with the 360° span of circumferential uniform heat flux compared with that of the absorber tubes modelled with the 160°, 180°, 200° and 240° span of non-uniform heat flux distributions is approximately the same. This indicates that, for the Reynolds number range considered in this study, the effective (average) internal heat transfer coefficient is not

affected by the exterior heat flux distribution, and that the traditional heat transfer correlations given in Table 6 could be used without modification to account for circumferential wall temperature variations.

Fig. 17 shows the variation of the inner-wall-to-fluid bulk temperature difference with the Reynolds number for the heat flux cases in Fig. 16. The average inner-wall-to-fluid bulk temperature difference for the absorber tube modelled with the 360° span of uniform heat flux where $C_R = 10$ was 57%, 64%, 67% and 71% higher than that of the absorber tubes modelled with 240°, 200°, 180°, and 160° spans of non-uniform heat flux distributions respectively. The inner-wall-to-bulk temperature difference is inversely related to the heat transfer coefficient and directly related to the heat flux losses, which indicates that the heat transfer coefficient increases with the decrease in the inner-wall-to-bulk temperature difference and heat flux losses and increases with the Reynolds number. Based on equation (10), the increase in the internal heat transfer coefficient with the Reynolds number is more influenced by the decrease in the inner-wall-to-fluid bulk temperature difference than that of the decrease in heat flux loss. However, the physical mechanism behind this could actually be due to the turbulent nature of the fluid particles with the increase in Reynolds number.

Fig. 18 gives the profile of the variation of the circumferential inner-wall-to-fluid bulk temperature difference with different Reynolds numbers for the 200° span distribution case of the heat flux with $C_R = 10$. The profile consists of two portions: the portion where the inner-wall-to-fluid bulk temperature difference is positive, which refers to the heat flux into the fluid, and where it is negative, which refers to the heat flux from the fluid. The circumferential inner-wall-to-fluid bulk temperature difference decreased with the increase in Reynolds number and is highest at the peak portion of the profile, which corresponds to the most heated lower central portion of the tube. It also decreased down to the unirradiated portion of the tube where it was negative for the thermal conductivity and tube-wall thickness

considered in this study. The circumferential internal heat transfer coefficient of the absorber tube, which is a function of the circumferential inner-wall heat flux of the tube and the circumferential inner-wall-to-fluid bulk temperature difference, would also vary along the circumferential inner-wall surface of the tube. At the unirradiated portion of the tube where the inner-wall-to-fluid bulk temperature difference is negative, it would also result in the negative heat transfer coefficient, which indicates that the tube is losing heat from the unirradiated portion and therefore is required to be insulated.

Fig. 19 presents the variations of the average overall heat transfer coefficients determined from eqn. (24), with the increase in Reynolds number for the heat flux cases in Fig. 16. As in the case of uniform heat flux with different C_R in Fig.15, the increase in the average overall heat transfer coefficient with the Reynolds number also had two parts: the first part with rapid increase, followed by the second part which nearly remained horizontal, indicating no further significant change in the average overall heat transfer coefficients with the increased Reynolds number. It also shows that the average overall heat transfer coefficient for the 360° span of uniform heat flux is higher than that of the 160°, 180°, 200°, and 240° span of sinusoidal non-uniform heat flux, which could be due to its higher heat flux of 7.1 kW/m² and the consequent increase in heat flux losses than of the non-uniform heat fluxes. For the circumferential non-uniform heat flux cases with the same effective average heat flux, the average overall heat transfer coefficients were approximately the same.

Fig. 20 shows the variation of the axial local internal heat transfer coefficient at the inlet Reynolds number of 4 000 along the tube, modelled with a 360° span of uniform heat flux and the 160°, 200° and 240° span of non-uniform heat flux distributions. The axial local internal heat transfer coefficient decreased with the increase along the length of the tube. The axial inner-wall-to-fluid bulk temperature difference shown in Fig. 21 is inversely related to the heat transfer coefficient. Therefore, the axial local internal heat transfer coefficient

decreased with the increase in the inner-wall-to-fluid bulk temperature difference as shown in Fig. 20, due to the increase in the fluid temperature along the tube length. As it could be expected, the axial local internal heat transfer coefficient was higher towards the inlet of the tube, where the thermal boundary layer was thinnest. As the thermal boundary increases and the flow become more developed, the heat transfer coefficient continued to decrease down to the tube length. However, the slight change in the decrease rate of the heat transfer coefficient could be due to the slight increase in heat transfer coefficient which occurred where the flow tends to depart from the region where the influence of the hydrodynamic and thermal boundary layer effect could be insignificant. The axial local internal heat transfer coefficient for the absorber tube modelled with a 360° span of uniform heat flux for the case where $C_R = 10$ was 0.64%, 0.61% and 0.53% higher than that of the absorber tubes modelled with the 160° , 200° and 240° span of circumferentially averaged non-uniform heat flux distributions respectively.

5.6 Heat transfer coefficients for the absorber tubes with different inner diameters and wall thicknesses

Fig. 22 presents the average internal heat transfer coefficient for four absorber tubes with different inner diameters and wall thicknesses, with thermal conductivity of 16.27 W/mK and modelled with a 200° span of the sinusoidal function of the flux in table 5 with $C_R = 10$. It shows that the average internal heat transfer coefficient of the tubes increased with the increase in mass flow rate of the heat transfer fluid and also increased with the decrease in the inner diameter and wall thickness of the tubes. The average internal heat transfer coefficient for the absorber tube with a 35.1 mm inner diameter and 3.56mm wall thickness was 24.74% higher than that of the absorber tube with a 40.9 mm inner diameter and a 3.68 mm wall thickness, 52.79% higher than that of the absorber tube with a 52.5 mm inner diameter and a 3.91 mm wall thickness, and 65.97% higher than that of the absorber tube with a 62.7 mm

inner diameter and a 5.16 mm wall thickness between the mass flow rate of 0.15 kg/s and 10 kg/s. The variations in the heat transfer coefficients of these tubes could be attributed to the difference in their conduction and convection thermal resistances resulting from the differences in their wall thicknesses and inner-wall diameters. These showed that the inner diameter and wall thickness of an absorber tube and mass flow rate of the heat transfer fluid have very important effects on the internal heat transfer coefficient of the tube. Fig. 22 shows that the heat transfer coefficient could be increased by decreasing the tube diameter at constant mass flow rate and also by increasing the mass flow rate at constant tube diameter. However, decreasing the absorber tube inner diameter to enhance the internal heat transfer coefficient would result in an increase in pressure drop, since pressure is inversely related to the tube diameter.

Fig. 23 shows the variations of the average overall heat transfer coefficients with the increase in mass flow rate of the heat transfer fluid for the absorber tubes in Fig. 22. It shows that the variation of the average overall heat transfer coefficient for the absorber tubes with different inner diameters and wall thicknesses also had two parts as in the cases of the uniform heat flux with different C_R in Fig. 15 and that of non-uniform heat flux of different angle spans of distributions in Fig. 19. The first part gave a rapid increase followed by the second part, which was almost horizontal, indicating that there was no significant change in the average overall heat transfer coefficient with the increase in mass flow rate of the heat transfer fluid. The average overall heat transfer coefficient increased with the decrease in the inner diameter and wall thickness of the absorber tubes with the same thermal conductivity of 16.27 W/mK. However, it was observed that the difference between the overall heat transfer coefficients of the tubes was decreasing as the mass flow rate of the heat transfer fluid kept increasing. This implies that the average overall heat transfer coefficients of absorber tubes

with different inner diameters and wall thicknesses, but with the same thermal conductivity and heat flux of the same concentration ratio are negligible at higher mass flow rate.

6. Conclusion

In this study the influence of concentrated circumferential solar heat flux distributions on the internal and overall heat transfer coefficients of linear Fresnel collector absorber tubes were numerically investigated. The tubes were modelled with a 360° span of circumferential uniform heat flux and 160°, 180°, 200° and 240° spans of sinusoidal circumferential non-uniform heat flux under steady-state and turbulent flow conditions. In both cases of the heat flux distributions, the average internal heat transfer coefficient for the absorber tubes considered increased with the increase in Reynolds number. It was found that the average internal heat transfer coefficients for the circumferential uniform heat flux with different concentration ratios were approximately the same, but the average overall heat transfer coefficient and the outlet temperature of the heat transfer fluid increased with the increase in the concentration ratios of the incident solar heat flux on the tubes. It was also found that the average internal heat transfer coefficient for the circumferential uniform heat flux compared with that of the sinusoidal circumferential non-uniform heat flux distributions on the absorber tube of the same inner diameter, wall thickness and thermal conductivity, was approximately the same as that of the non-uniform heat flux distribution cases of a lower average heat flux than that of the circumferential uniform heat flux. This indicated that the average internal heat transfer coefficient was not affected by the exterior heat flux distribution; but the average overall heat transfer coefficient for the circumferential uniform heat flux was greater than that of the non-uniform heat flux due to its higher heat flux. The average internal and overall heat transfer coefficients were found to increase with the decrease in the inner diameter and the wall thickness of the absorber tubes of the same thermal conductivity. However, decreasing the absorber tube inner diameter to enhance the internal heat transfer

coefficient would result in the increase in pressure drop, since pressure is inversely related to tube diameter.

Acknowledgements

The funding obtained from the NRF, TESP, Stellenbosch University, University of Pretoria, SANERI/SANEDI, CSIR, EEDSM Hub and NAC is acknowledged and duly appreciated.

References

Abbas R., Montes M.J., Piera M. and Martinez-Val M., 2012a. Solar radiation concentration features in Linear Fresnel Reflector arrays. *Energy Conversion and Management*. 54, 133–144.

Abbas R., Muñoz J., Martínez-Val J.M., 2012b. Steady-State Thermal Analysis of an Innovative Receiver for Linear Fresnel Reflectors. *Renewable Energy*. 39, 198-206.

ANSYS Fluent version 14.0, 2011. Users' Guide ANSYS, Release 14.0 Incorporated, Southpointe 275 Technology Drive Canonsburg, PA 15317.

Barale G., Heimsath A., Nitz P. and Toro A., (2010). Optical Design of a Linear Fresnel Collector for Sicily, Solar PACE, Fabbrica Energie Rinnovabili Alternative srl, Milano, Italy.

Cengel Y. A., 2007. *Heat and Mass Transfer: A Practical Approach*, 3rd ed. Published by McGraw-Hill Companies, Inc. 1221 Avenue of the Americas, New York, NY 10020.

Cheng Z.D., He Y.L., Cui F.Q., Xu R.J. and Tao Y.B., 2012. Numerical Simulation of a Parabolic Trough Solar Collector with Non-uniform Solar Flux Conditions by Coupling FVM and MCRT Method Solar Energy. 86 , 1770–1784.

Dey C.J., 2004. Heat Transfer Aspects of an Elevated Linear Absorber. Solar Energy. 76: 243–249.

Duffie J. A. and Beckman W. A. 1980. Solar Engineering of Thermal Processes. Second Edition. A Wiley-Interscience Publication, John Wiley & Sons, Inc. New York.

Eck M., Uhlig R., Mertins M., Häberle A. and Lerchenmüller H., 2007. Thermal Load of Direct Steam-Generating Absorber Tubes with Large Diameter in Horizontal Linear Fresnel Collectors, Heat Transfer Engineering . 28 (1), 42-48.

Ferziger J.H. and Perifi M., 2002. Computational Methods for Fluid Dynamics, 3 Rev. ed.- Berlin; Heidelberg; Hong Kong; London; Milan; Paris; Tokyo: Springer .

Francisco J., Rosario C., Juan R.L., Felipe R., José G., 2011. Experimental validation of an optical and thermal model of a Linear Fresnel Collector. 2nd European Conference on Polygeneration –Tarragona, Spain: 1-8.

Goswami R.P., Negi B.S., Sehgal, H.K. and Sootha G.D., 1990. Optical Designs and Concentration Characteristics of a Linear Fresnel Reflector Solar Concentrator with a Triangular Absorber. Solar Energy Materials. 21, 237-251. North-Holland.

Grena R., 2010. Optical Simulation of a Parabolic Solar Trough Collector. *International Journal of Sustainable Energy*. 29 (1), 19–36.

Häberle A., Zahler C., Lerchenmüller H., Mertins M., Wittwer C., Trieb F. and Dersch J., 2002. The Solarmundo Line Focussing Fresnel Collector: Optical and Thermal Performance and Cost Calculations. Solar PACES, Switzerland.

Kalogirou S.A., 2004. Solar Thermal Collectors and Applications. *Progress in Energy and Combustion Science*. 30: 231–295.

Krothapalli A. and Greska B. (nd) Concentrated Solar Thermal Power. Department of Mechanical Engineering, Florida State University, Tallahassee, FL 32310, Sustainable Energy Technologies, LLC St. Cloud, FL 34771.

Mathur S.S., Kandpal T.C. and Negi B.S., 1991. Optical Design and Concentration Characteristics of Linear Fresnel Reflector Solar Concentrators - II. Mirror Elements of Equal Width. *Energy Convers. Management*. 31(3): 221-232.

Mehmet K. and Tiirkan K., 1997. Numerical Simulation of a Gaseous Fueled (Methane) Combustor. *Mathematical and Computational Applications*. 2 (3), 101-118.

Mills D.R. and Morrison G.L., 1999. Modelling Study for Compact Fresnel Reflector Power Plant. *Journal of Phys. IV France* 9. 159-165.

OneSteel Building Services, 2003. Doc. Ref 067 Jan 03, Adelaide 70 Grand Junction Road, Kilburn S A. www.OneSteelBuildingServices.com.

Patankar S.V., 1980. Numerical Heat Transfer and Fluid Flow. Hemisphere Publishing Corporation, United States of America.

Peter H., 2008. Task III: Solar Technology and Advanced Applications. Annual Report, Solarpaces . 7-10.

Pino F.J., Caro R., Rosa F., Guerra J., 2012. Experimental Validation of an Optical and Thermal Model of a Linear Fresnel Collector System. Applied Thermal Engineering xxx.1-9.

Rajput R.K., 2005. Heat and Mass Transfer in SI Units. Second Edition. Published by S. Chand and Company Ltd, Ram Nagar, New Delhi - 110 055.

Tiwari G.N., 2006. Solar Energy Fundamental, Design, Modelling and Applications. Narosa Publishing House, 22 Daryaganj, Delhi, India.

Velázquez N., García-Valladares O., Saucedo D. and Beltrán R., 2010. Numerical simulation of a Linear Fresnel Reflector Concentrator used as direct generator in a Solar-GAX cycle. Energy Conversion and Management. 51, 434–445.

Versteeg H.K. and Malalasekera W., 1995. An Introduction to Computational Fluid Dynamics: The Finite Volume Method. Longman Scientific and Technical, Longman House, Burnt Mill, Harlow Essex CM20 2JE, England.

Vikram R., Snehamoy M. and Dipankar S., 2010. Analysis of the Turbulent Fluid Flow in an Axi-symmetric Sudden Expansion. *International Journal of Engineering Science and Technology*. 2(6),1569-1574.

Warwick J. and Middleton P., 2012. Construction of first SA-developed CSP Plant begins. *Mechanical Technology*, Crown Publications CC, Crown House, Cnr Theunis and Sovereign Street, Bedford Gardens. 20 – 21.

Yildiz E., Dost S. and Yildiz M., 2006. A numerical simulation study for the effect of magnetic fields in liquid phase diffusion growth of SiGe single crystals. *Journal of Crystal Growth*. 291, 497–511.

List of figures

Fig. 1. Linear Fresnel concentrating solar collector with compound parabolic receiver cavity

Fig. 2. Linear Fresnel concentrating solar collector with trapezoidal receiver cavity

Fig. 3. Absorber tube model divided into $M \times N$ numerical surfaces

Fig. 4. A cross-section of the absorber tube model

Fig. 5. Control volume (CV) of the element at location (m, n)

Fig. 6. Nusselt number from the ANSYS Fluent for 360° uniform heat flux and that of standard empirical correlations in table 6

Fig. 7. Temperature contours of the absorber tubes simulated with circumferential heat flux distributions.

Fig. 8 Non-uniform temperature factor for the non-uniform heat flux distributions

Fig. 9. Total surface heat flux contours for uniform and non-uniform heat flux distributions

Fig. 10. Sinusoidal circumferential heat flux distribution profile

Fig. 11. Non-uniform circumferential inner-wall heat flux distribution profile

Fig. 12. Average internal heat transfer coefficient for 360° span of circumferential uniform heat flux distributions.

Fig. 13. Average inner-wall-to-fluid bulk temperature difference with the Reynolds number

Fig. 14. Outlet temperatures of the heat transfer fluid of the absorber tubes in Fig. 12

Fig. 15. Average overall heat transfer coefficients for the absorber tubes in Fig. 12

Fig. 16. Average internal heat transfer coefficients for circumferential uniform and non-uniform heat flux distributions

Fig. 17. Inner-wall-to-fluid bulk temperature difference for the absorber tubes with circumferential uniform and non-uniform heat flux distributions

Fig. 18. Circumferential variation of the inner-wall-to-fluid bulk temperature difference

with the Reynolds number

Fig. 19. Average overall heat transfer coefficients for the heat flux cases in Fig. 16

Fig. 20. Axial local internal heat transfer coefficient for 10 m long absorber tubes with circumferential uniform and non-uniform heat flux distributions for an inlet Reynolds number of 4 000

Fig.21. Axial inner-wall-to-fluid bulk temperature difference of 10 m long absorber tubes with circumferential uniform and non-uniform heat flux distributions

Fig. 22. Average internal heat transfer coefficient for four absorber tubes of different inner-wall diameters and wall thicknesses

Fig.23. Average overall heat transfer coefficients for the absorber tubes in Fig.22

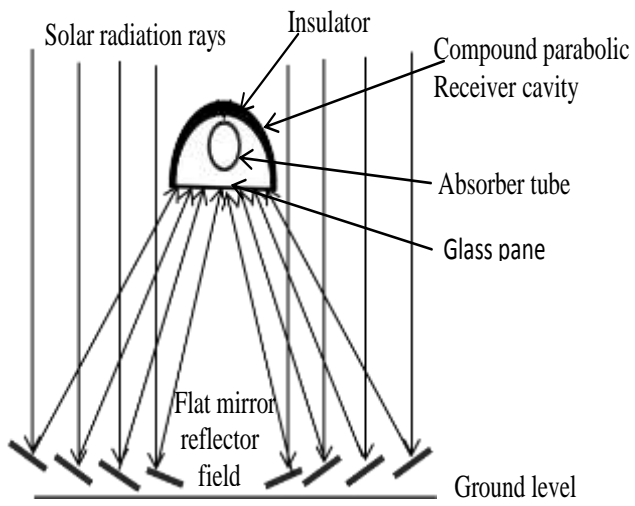


Fig.1

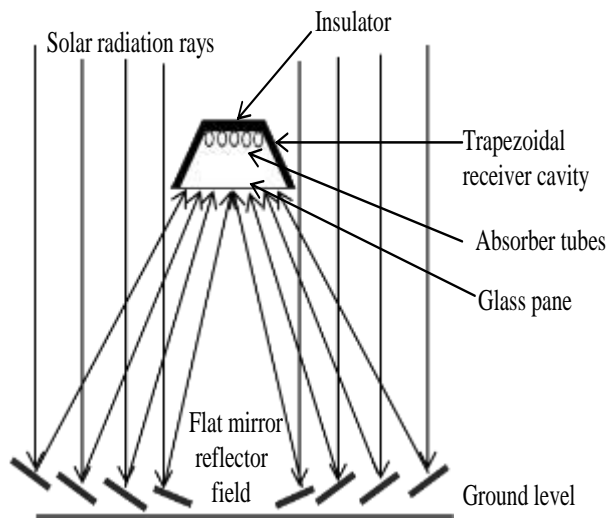


Fig. 2

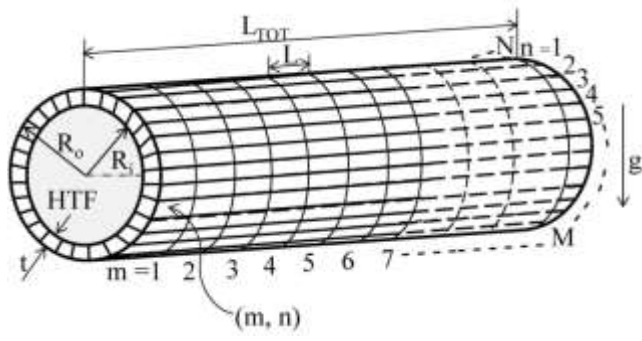


Fig.3

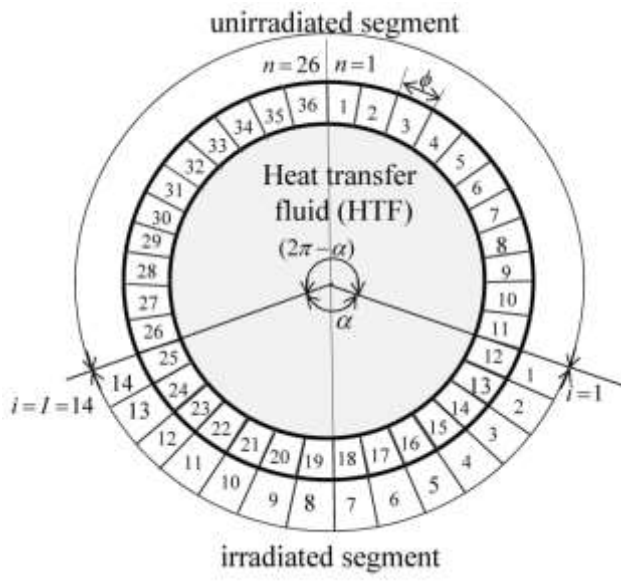


Fig. 4

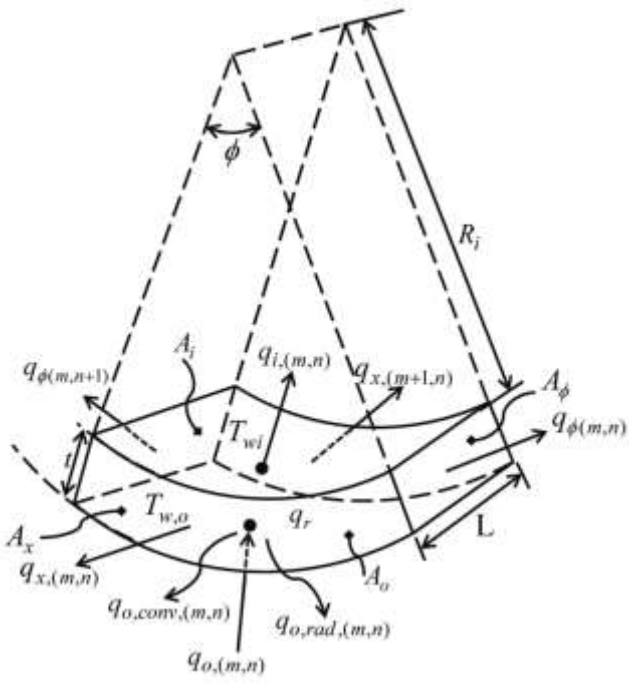


Fig.5

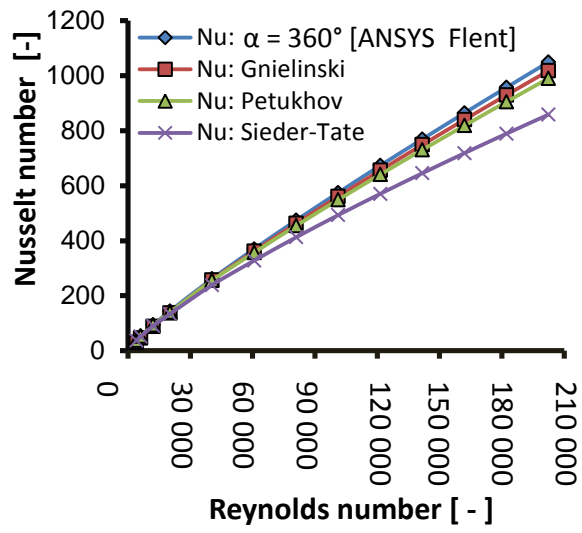


Fig. 6

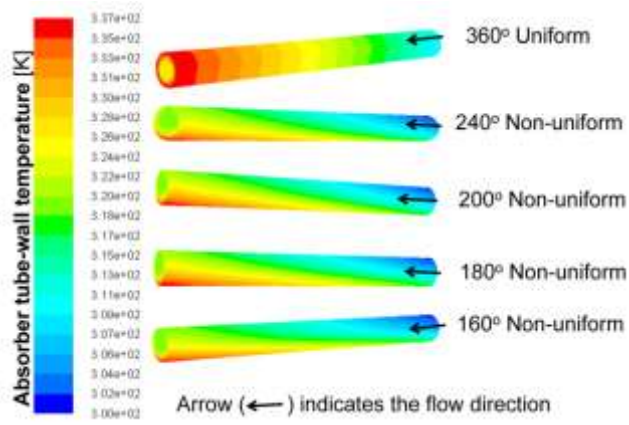


Fig. 7

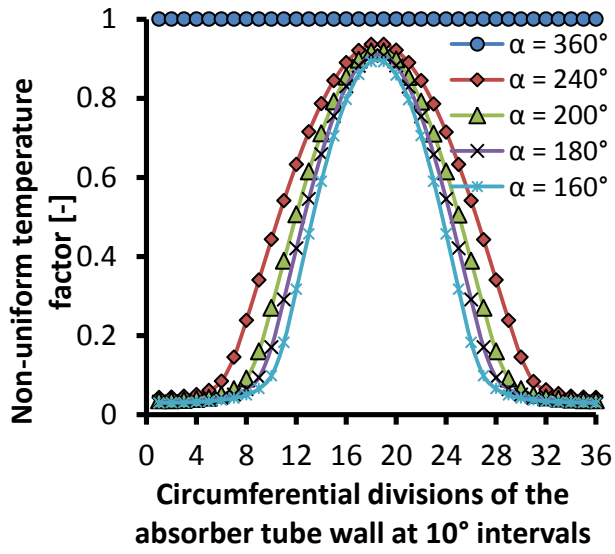


Fig. 8

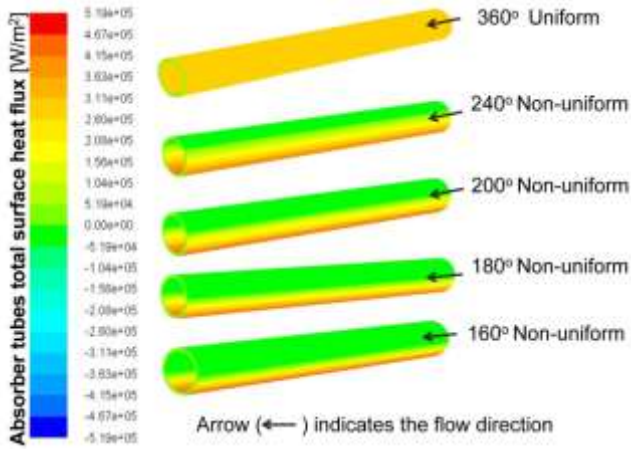


Fig. 9.

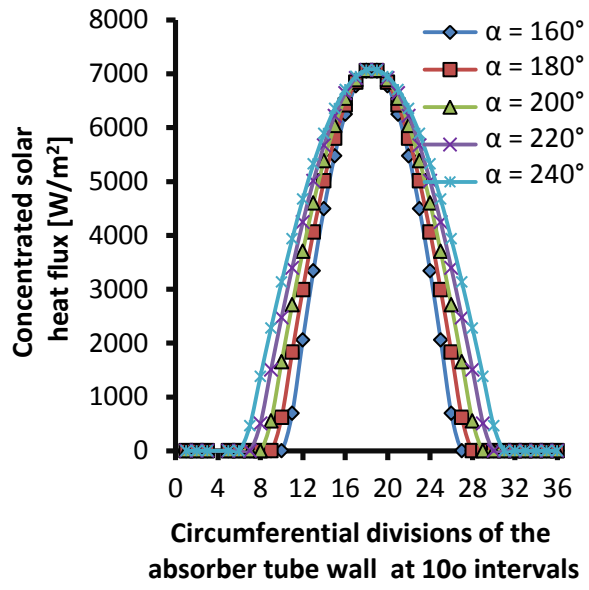


Fig. 10

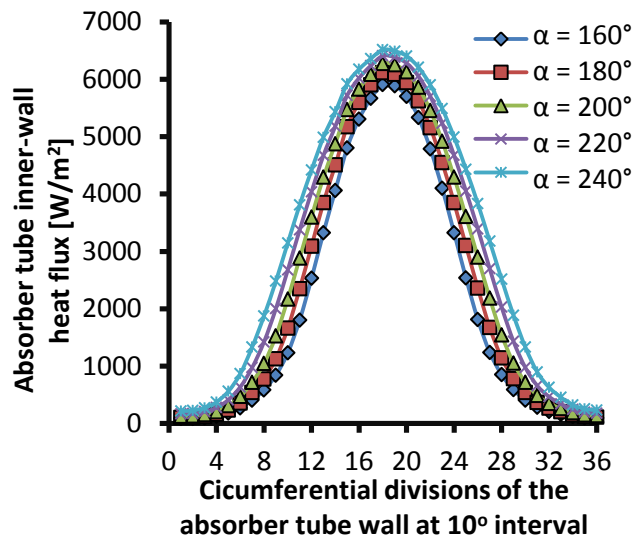


Fig. 11

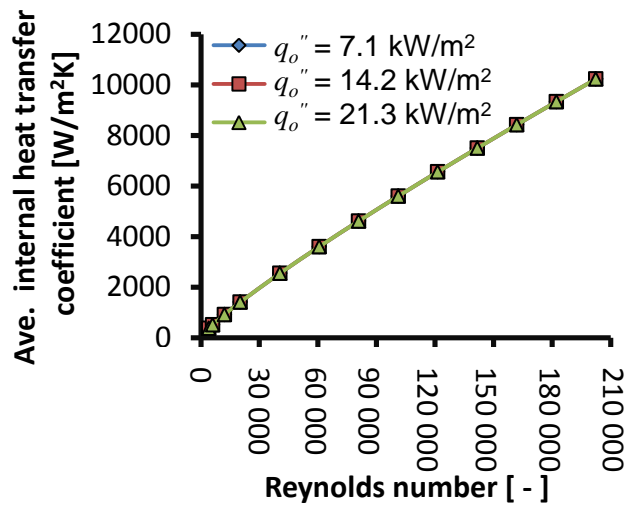


Fig. 12

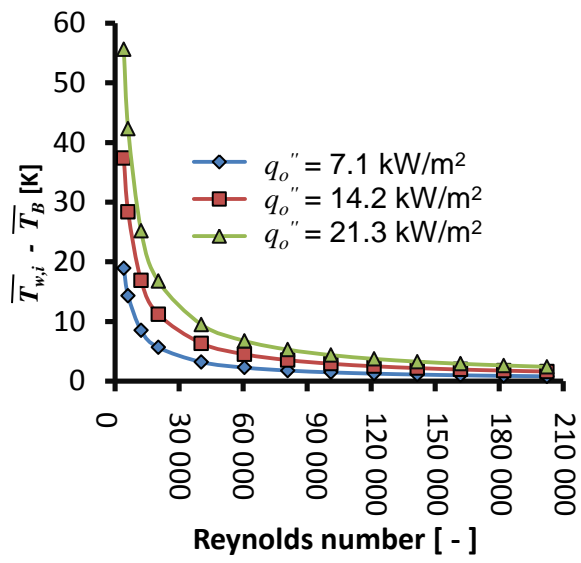


Fig. 13

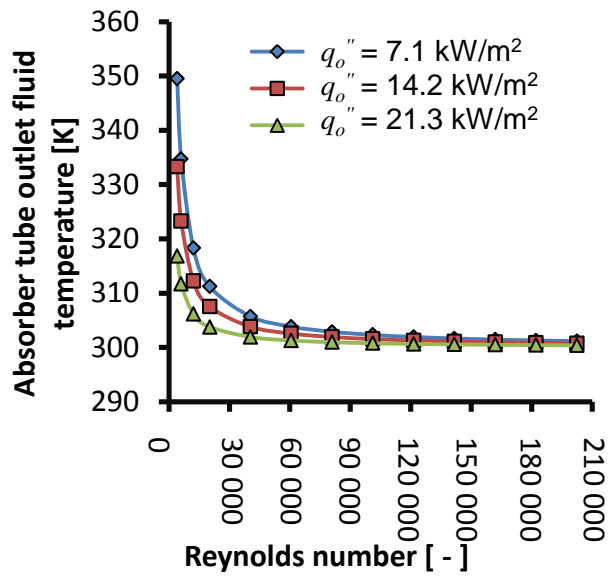


Fig. 14

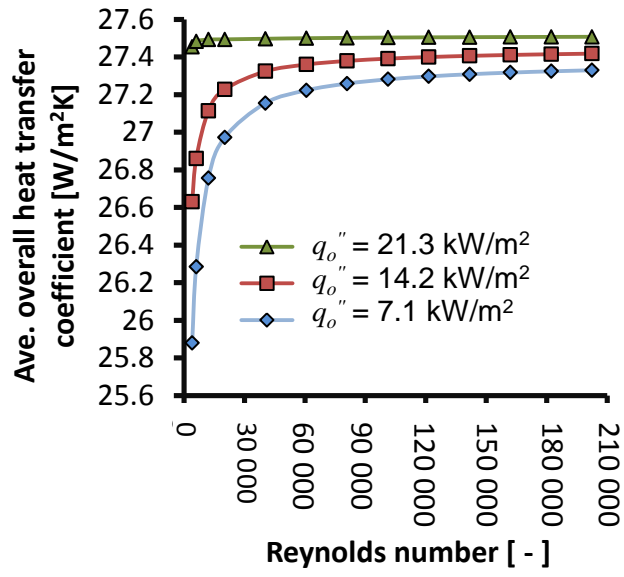


Fig. 15

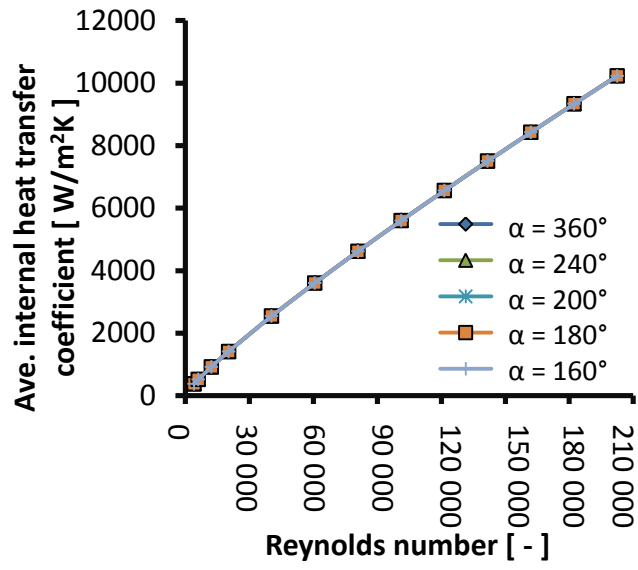


Fig. 16

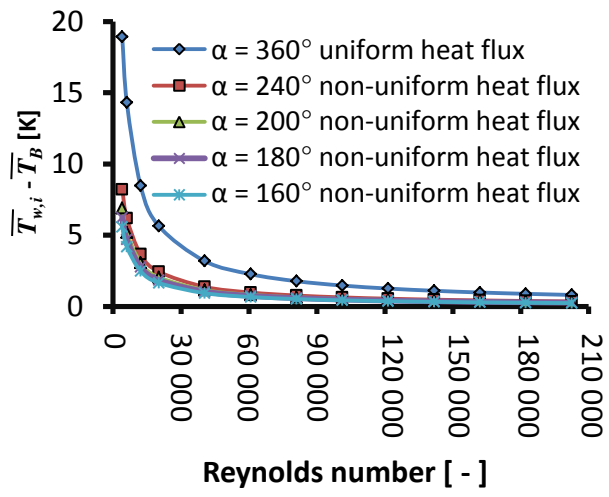


Fig. 17

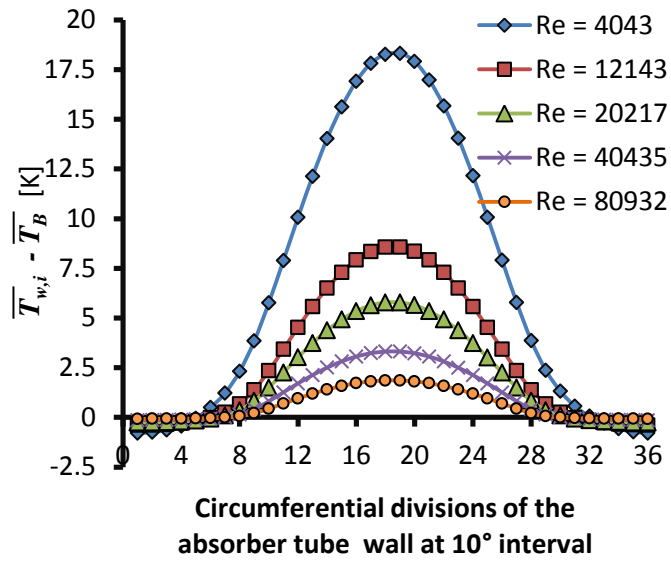


Fig. 18

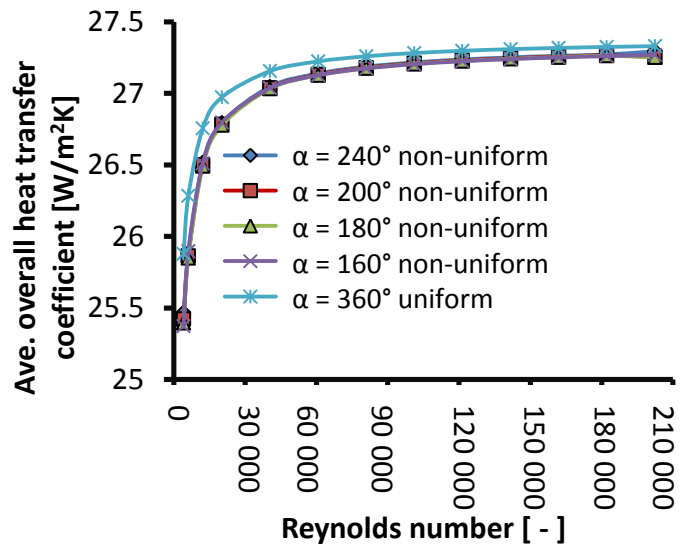


Fig. 19

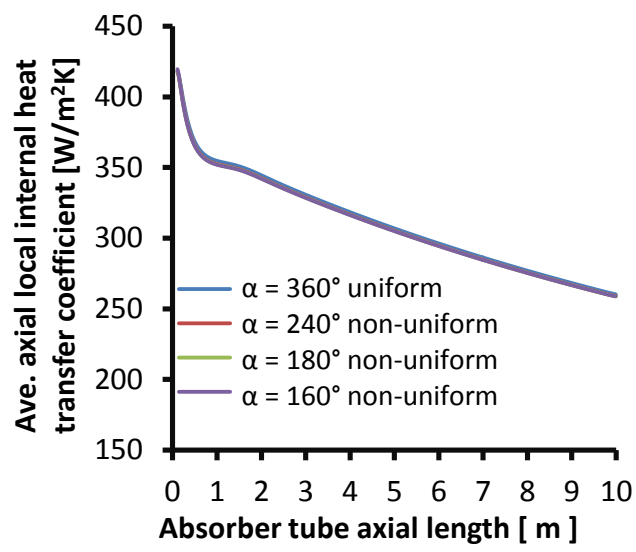


Fig. 20

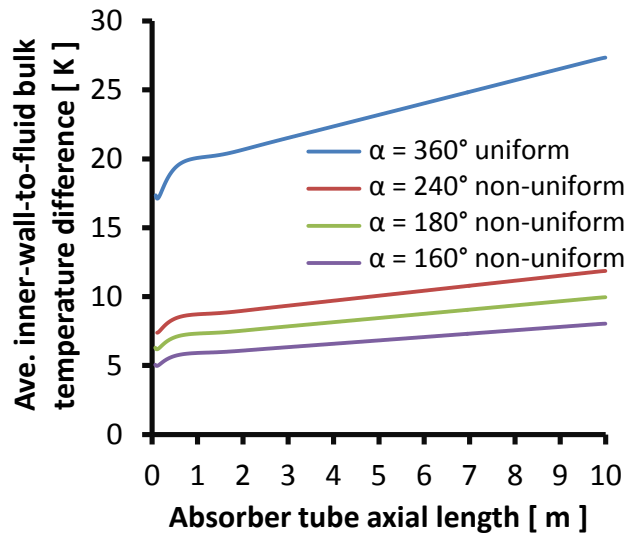


Fig.21

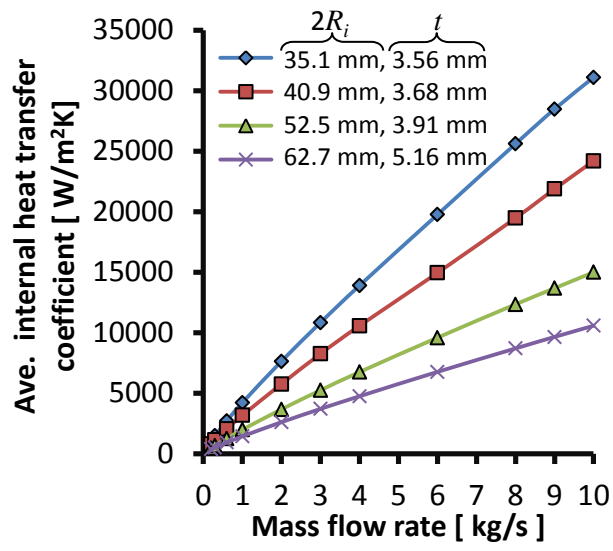


Fig. 22

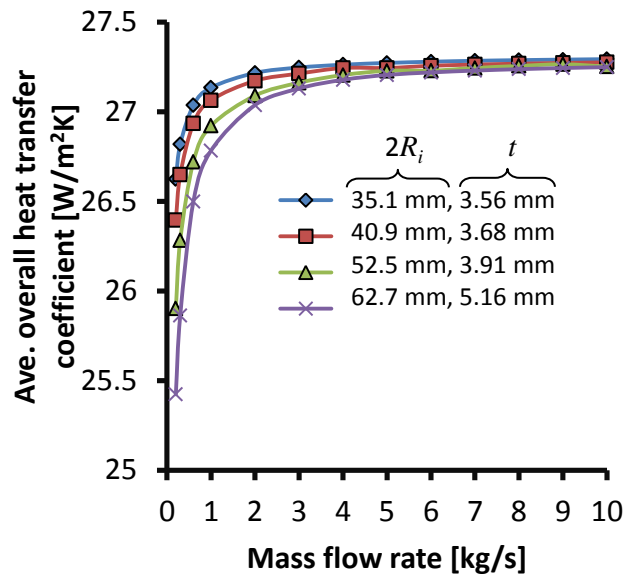


Fig. 23

List of Tables

Table 1 Convection-diffusion equation variables

Table 2 Grid refinement test results

Table 3 Geometrical parameters of the absorber tubes

Table 4 Properties of the heat transfer fluid and absorber tube material

Table 5 Solar heat flux and concentrating collector parameters

Table 6 Standard empirical correlations of Nusselt numbers, \overline{Nu}_i

Table 1

Equation	ϕ	Γ_ϕ	S_ϕ
Continuity	1	0	0
r-momentum	v_r	μ_{ef}	$-\frac{\partial p}{\partial r} + \mu_{ef} \left[-\frac{v_r}{r^2} - \frac{2}{r^2} \frac{\partial v_\phi}{\partial \phi} \right] + \frac{v_\phi}{r} + g_r \beta$
ϕ - momentum	v_ϕ	μ_{ef}	$-\frac{1}{r} \frac{\partial p}{\partial \phi} + \mu_{ef} \left[-\frac{v_\phi}{r^2} + \frac{2}{r^2} \frac{\partial v_r}{\partial \phi} \right] - \frac{v_\phi v_r}{r} + g_\phi \beta$
x-momentum	v_x	μ_{ef}	$-\frac{\partial p}{\partial r} + g_x \beta$
Energy	T	$\mu_l + \frac{\mu_{ed}}{\sigma_{ed}}$	0
k - turbulence	k	$\mu_l + \frac{\mu_{ed}}{\sigma_k}$	$G - \rho \varepsilon$
ε - turbulence	ε	$\mu_l + \frac{\mu_{ed}}{\sigma_\varepsilon}$	$\frac{\varepsilon}{k} (C_1 G - C_2 \rho \varepsilon)$

Table 2

Number of numerical cells	Bulk fluid outlet temperature (K)	Change in outlet temperature due to refinement
145688	306.1629	-
327000	306.1656	0.0027
436218	306.1666	0.001
585117	306.1657	0.0009
652000	306.1653	0.0004

Table 3

Outer diameter [m]	Inner diameter [m]	Thickness, t [m]	Length, L_{TOT} [m]
0.0422	0.0351	0.00356	10
0.0483	0.0409	0.00368	10
0.0603	0.0525	0.00391	10
0.0730	0.0627	0.00516	10

Table 4

Property	Heat transfer fluid (water)	Steel absorber tube
Density [kg/m ³]	998.2	8030
Specific heat capacity [J/kgK]	4182	502.48
Thermal conductivity [W/mK]	0.61	16.27
Viscosity [Ns/m ²]	0.001003	-
HTF temperature [K]	300	-
Emissivity of the absorber tube [-]	-	0.85

Table 5

Concentratio r factor, C_R [-]	Tube absorptivity, α_{tu} [-]	Mirror reflectivity, γ_{mi} [-]	Beam solar heat flux , q_{DNI}'' [W/m ²]	Concentrated solar heat flux, $q_{o(m,n)}''$ [W/m ²]
10	0.90	1	787.263	7, 085
20	0.90	1	787.263	14, 170
30	0.90	1	787.263	21, 256

Table 6

Gnielinski correlation	$\overline{Nu}_i = \frac{\left(\frac{f}{8}\right)(Re-1000)Pr}{1+12.7(f/8)^{0.5}(Pr^{2/3}-1)}$ $f = (0.790 \ln Re - 1.64)^{-2}$	$\left(\begin{array}{l} 0.5 \leq Pr \leq 2000 \\ 3 \times 10^3 < Re < 5 \times 10^6 \end{array} \right)$ $(10^4 < Re < 10^6)$
Sieder-Tate correlation	$\overline{Nu}_i = 0.027 Re^{4/5} Pr^{1/3} \left(\frac{\mu_b}{\mu_w}\right)^{0.14}$	$\left(\begin{array}{l} 0.7 \leq Pr \leq 16,700 \\ Re \geq 10,000 \end{array} \right)$
Petukhov correlation	$\overline{Nu}_i = \frac{\left(\frac{f}{8}\right) Re Pr}{1.07 + 12.7(f/8)^{0.5}(Pr^{2/3}-1)} \left(\frac{\mu_b}{\mu_w}\right)^n$ $n = 0.11 \text{ for heating and } 0.25 \text{ for cooling.}$	$\left(\begin{array}{l} 0.7 \leq Pr \leq 16,700 \\ Re \geq 10,000 \end{array} \right)$